RESEARCH ARTICLE

Structure of the Cytochrome b_6f Complex of Oxygenic Photosynthesis: Tuning the Cavity

Genji Kurisu,[1,2]* Huamin Zhang,[1]* Janet L. Smith,[1] William A. Cramer[1]†

The cytochrome b_6f complex provides the electronic connection between the photosystem I and photosystem II reaction centers of oxygenic photosynthesis and generates a transmembrane electrochemical proton gradient for adenosine triphosphate synthesis. A 3.0 angstrom crystal structure of the dimeric b_6f complex from the thermophilic cyanobacterium *Mastigocladus laminosus* reveals a large quinone exchange cavity, stabilized by lipid, in which plastoquinone, a quinone-analog inhibitor, and a novel heme are bound. The core of the b_6f complex is similar to the analogous respiratory cytochrome bc_1 complex, but the domain arrangement outside the core and the complement of prosthetic groups are strikingly different. The motion of the Rieske iron-sulfur protein extrinsic domain, essential for electron transfer, must also be different in the b_6f complex.

In oxygenic photosynthesis, three integral membrane protein complexes accomplish electron transport and generate the transmembrane electrochemical proton gradient used for energy transduction (Fig. 1). Light energy transferred to the photosystem I and II reaction centers (PSI and PSII) activates electron transfer (*1*). The cytochrome b_6f complex mediates electron transfer between the reaction centers by oxidizing lipophilic plastoquinol and reducing plastocyanin or cytochrome c_6 (*2–4*). Three-dimensional structures exist for PSI at 2.5 Å (*5*) and PSII at 3.7 Å (*6*, *7*). Determination of the 3.0 Å crystal structure of the cytochrome b_6f complex completes the description of the architecture of energy transduction in oxygenic photosynthesis.

Within the b_6f complex, one electron is transferred from doubly reduced dihydroplastoquinone (PQH_2) to a high-potential electron transfer chain, consisting of the Rieske iron-sulfur protein and cytochrome f on the electropositive side of the membrane (Fig. 2A). This results in the release of two protons to the aqueous lumen phase. Transfer of the second electron from PQH_2 across the complex through two b hemes (*8–11*), or as anionic plastosemiquinone (*12*), and the resulting proton uptake from the electronegative side generate a proton electrochemical gradient across the membrane.

Electron transfer and proton translocation functions similar to those in the cytochrome b_6f complex are performed by the respiratory cytochrome bc_1 complex, using the two b hemes, one high-potential c heme (cytochrome c_1, functionally analogous to cytochrome f), one [2Fe-2S] cluster, and dihydroubiquinol/ubiquinone. Lipophilic quinone species from the bulk membrane bilayer phase move between a site for reduction and proton uptake on the electronegative (*n*) side of the membrane and a site for oxidation and proton release on the electropositive (*p*) side. The b_6f and bc_1 complexes share the basic elements of this process, which is explained by a Q (quinone)–cycle mechanism (*8–11*). A structural framework for the Q cycle is provided by the two large central cavities in crystal structures of the dimeric bc_1 complex from bovine (*13–16*), avian (*14*), and yeast (*17*) sources. Each cavity connects ubiquinone-reactive sites containing hemes b_p and b_n on the *p* and *n* sides of the complex.

The cytochrome b_6f complex from *Mastigocladus laminosus*, a thermophilic cyanobacterium, contains four large subunits (18 to 32 kD), including cytochrome f, cytochrome b_6, the Rieske iron-sulfur protein (ISP), and subunit IV; as well as four small hydrophobic subunits, PetG, PetL, PetM, and PetN, leading to a dimer molecular weight of 217 kD (*18*). Crystal structures are available for the extrinsic soluble domains of cytochrome f (*19–21*) and the ISP (*22*). Cytochrome b_6 and subunit IV are homologous to the N- and C-terminal halves of cytochrome b of the bc_1 complex (*23*), as is the ISP between the two complexes (*22*). However, the c-type cytochrome f of the b_6f complex is unrelated to cytochrome c_1 of the bc_1 complex (*19*).

Structure determination. Growth of diffraction-quality crystals of the cytochrome b_6f complex required augmentation of the detergent-solubilized preparation with synthetic lipid [dioleoylphosphatidyl-

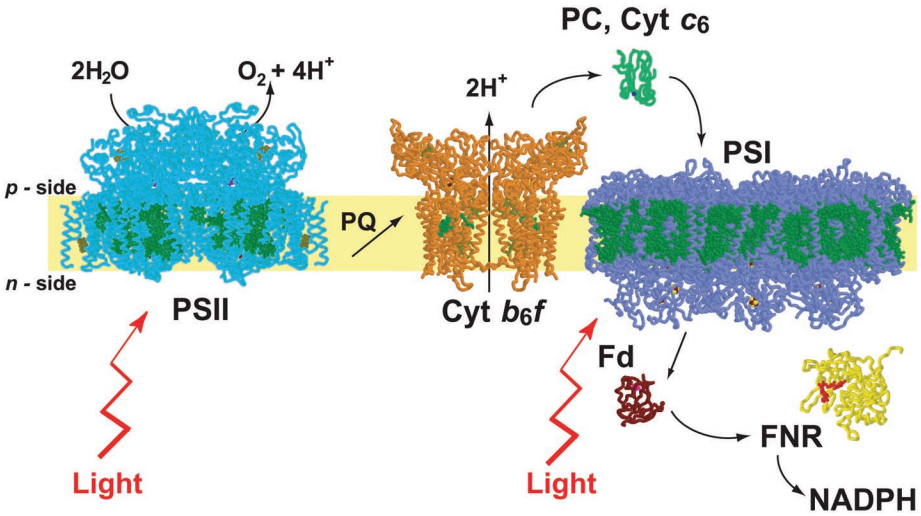

Fig. 1. The integral membrane protein complexes responsible for electron transport and proton translocation in oxygenic photosynthesis. The structures are from thermophilic cyanobacterial sources: *S. elongatus* for the reaction centers of PSI [purple; Protein Data Bank (PDB) accession code 1JB0] and PSII (cyan; PDB accession code 1IZL), and *M. laminosus* for the cytochrome b_6f complex (orange), described in the present work. Lumen (*p*) and stromal (*n*) -side soluble electron transfer proteins are plastocyanin (green) or cytochrome c_6, ferredoxin (dark brown), and ferredoxin:$NADP^+$ reductase (yellow).

[1]Department of Biological Sciences, 915 West State Street, Purdue University, West Lafayette, IN 47907–2054, USA. [2]Institute for Protein Research, Osaka University, Suita, Osaka 565–0871, Japan.

*These authors contributed equally to this work.
†To whom correspondence should be addressed. E-mail: wac@bilbo.bio.purdue.edu

choline (DOPC)] (*24*). The structure was solved by isomorphous replacement using Pb and Pt derivatives and multiwavelength anomalous diffraction from native iron atoms (table S1). The initial model was built into a 3.4 Å map of the native complex. Refinement was carried out with a 3.0 Å data set from a co-crystal with the quinone-analog inhibitor tridecylstigmatellin (TDS) (Table 1).

Overall structure. All four large and four small subunits of each monomer were positioned in the 3.0 Å electron density map without ambiguity. The monomer includes four hemes, one [2Fe-2S] cluster, one chlorophyll a, one β-carotene, one plastoquinone, one added quinone-analog inhibitor, TDS, and two added DOPC lipids (Fig. 2B). The monomeric unit contains 13 transmembrane helices: four in cytochrome b_6 (helices A to D); three in subunit IV (helices E to G); and one each in cytochrome f, the ISP, and the four small hydrophobic subunits PetG, -L, -M, and -N (Fig. 2, A and C). The extrinsic domains of cytochrome f and the ISP are on the *p* side of the membrane (Fig. 2A) and are ordered in the crystal structure. Loops and chain termini on the *n* side are less well ordered. The model has no internal gaps for any of the 16 subunits of the dimer, but a total of 128 terminal residues are missing. Only the large extrinsic *p*-side domain of cytochrome f and *n*-side chain termini form crystal lattice contacts. The ISP contributes to dimer stability by domain swapping: Its

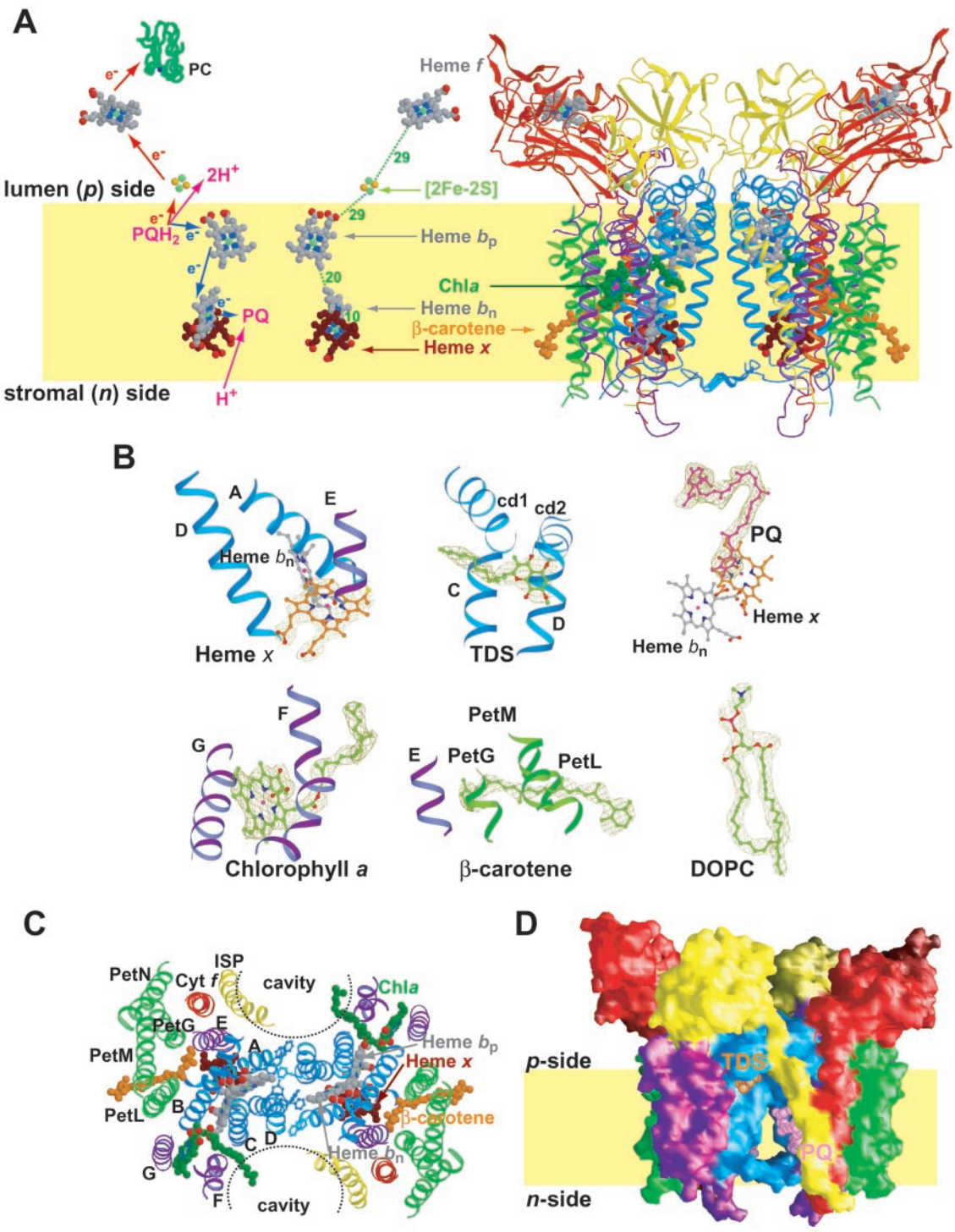

Fig. 2. The eight-subunit dimeric cytochrome b_6f complex. (**A**) (Left) Electron and proton transfer pathway through the b_6f complex and distances between redox cofactors. (Right) Side view showing bound cofactors and protein subunits. The color code is as follows: Cytochrome b_6 (blue); subunit IV (purple); cytochrome f (red); ISP (yellow); PetG, -L, -M, and -N (green); and the membrane bilayer (yellow band). (**B**) Electron density (RMSD level of the 2Fo-Fc map) of prosthetic groups, heme *x*, TDS, plastoquinone, chlorophyll a (Chla), β-carotene, and DOPC. (**C**) View normal to the membrane plane of the 26 transmembrane helices in the dimer; the color code is as in (A). The dimer interface is enriched in aromatic residues Phe^{52}, Phe^{56}, and Phe^{189} in the A and D helices of cytochrome b_6. Central cavities formed at the dimer interface are indicated by dotted lines. (**D**) Molecular surface of the complex showing the central quinone exchange cavity, including plastoquinone (magenta) and TDS (orange).

transmembrane helix obliquely spans the membrane in one monomer, and its extrinsic domain is part of the other monomer (Fig. 2, A and D).

Viewed normal to the membrane plane (Fig. 2C), the b_6f complex has dimensions of 90 × 55 Å within the membrane bilayer and on the *n* side, and of 120 × 75 Å on the *p* side. The complex extends 100 Å along the membrane normal. The transmembrane domains of the b_6f complex obey molecular twofold symmetry. Cα atoms of the transmembrane helices superimpose, with a root mean square deviation (RMSD) of 0.7 Å. The topologies of the subunits of the b_6f complex obey the cis-positive rule for integral membrane proteins (*25*). A pronounced asymmetry in the surface potential of the complex is produced by the basic *n* side and the anionic *p* side that results from the acidic cytochrome f and ISP.

The two monomers form a protein-free central cavity on each side of the transmembrane interface (Fig. 2D). Each cavity is 30 Å high, 15 Å deep, and 25 Å wide at its base near the *n*-side aqueous interface. Cavity walls are formed by helices C, D, and F of one monomer and by helices A and E and the ISP transmembrane helix of the other. The floor of the cavity is formed by the N-terminal 25 residues of cytochrome b_6 and, presumably, by lipid head groups that fill the cavity in situ. The narrow 13 × 13 Å roof of the cavity is formed by cd1 and cd2 *p*-side short peripheral helices connecting helices C and D of cytochrome b_6 and the C terminus of the ISP transmembrane helix. A small portal (11 × 12 Å) in the wall of each cavity is formed by helices C, cd1, and F, and leads to a *p*-side antechamber, or "Q_p pocket," in each monomer. The Q_p pocket is bounded by the [2Fe-2S] cluster, heme b_p and the "ef loop" connecting helices E and F of subunit IV.

Each monomer of the b_6f complex contains four heme cofactors and one [2Fe-2S] cluster (Fig. 2A). The two hemes of cytochrome b_6 (Fig. 3A), the c-type heme of cytochrome f, and the [2Fe-2S] cluster of the ISP are well-studied redox cofactors of the b_6f complex and are common to the b_6f and bc_1 complexes. Hemes b_p and b_n are bis-histidine-coordinated by imidazole side chains separated by 13 and 14 residues in the B and D helices, effectively cross-linking these two helices (*23*).

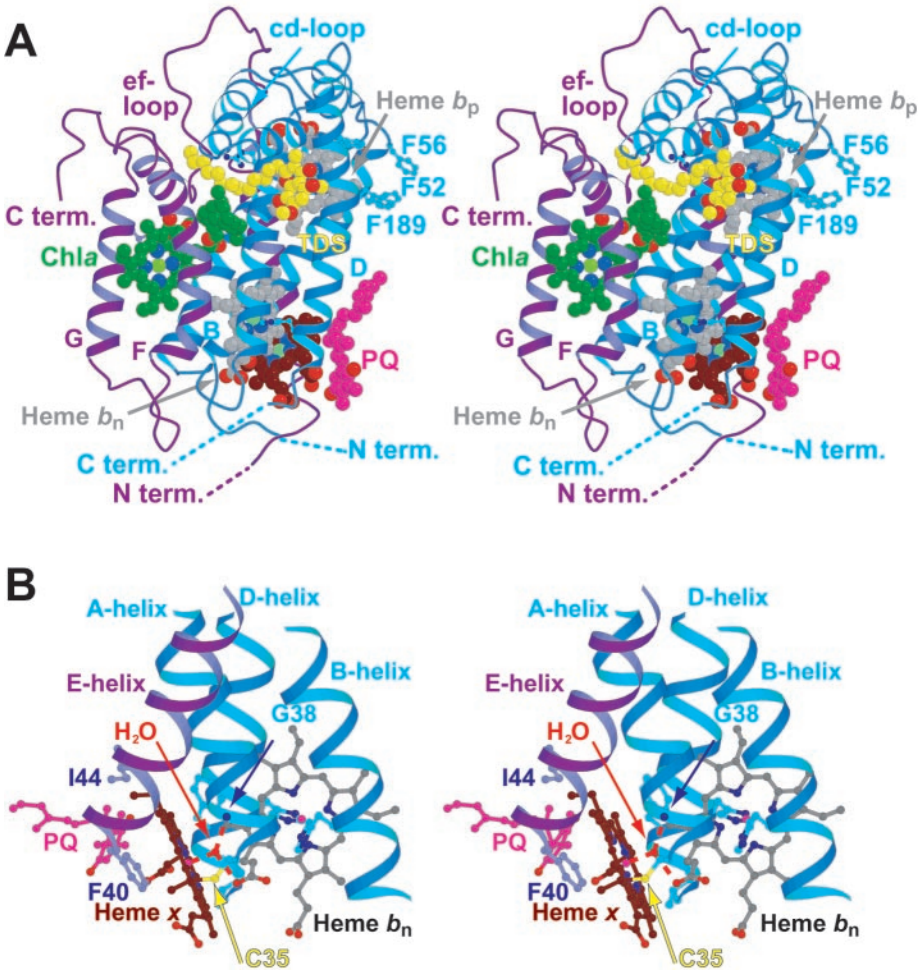

Fig. 3. Stereo views of the intramembrane core and bound molecules. (**A**) Side view. The two b hemes (gray) are bis-histidine-coordinated on the *n* and *p* sides of the B and D helices (blue). Chlorophyll a (green) is sandwiched between the F and G helices of subunit IV; the 20-carbon phytyl chain (green) extends normal to the figure into the *p* side of the quinone exchange cavity. Heme *x* (red-brown), ligated by water and the heme b_n propionate, lines the quinone exchange cavity, in contact with plastoquinone (magenta) near the *n* side of the cavity. TDS (yellow) is near the *p* side. (**B**) Linkage and coordination of heme *x*. Colors are as in (A); Cys^{35} (yellow) on the *n* side of the A helix makes the single covalent thioether bond with heme *x*. The fifth ligand is a water that is hydrogen-bonded (dashed line) to a heme b_n propionate. Phe^{40}, on the *n* side of the E helix, is parallel to heme *x* and near (6 to 9 Å) plastoquinone (PQ, magenta) in the cavity.

New heme *x*. A surprise of the crystal structure is an additional, unique heme (Fig. 3B and fig. S2) closely linked to heme b_n.

The flat shape of the electron density (Fig. 2B) at 3.0 Å resolution and a strong peak (4.8σ) in the iron anomalous-difference map implied a heme with a central Fe atom at a position between heme b_n and the central cavity. [The new heme was first identified in the structure of the b_6f complex of *Chlamydomonas reinhardtii* (*26*).] The new heme appears not to belong to a known heme family, and we therefore propose the temporary nomenclature "heme *x*". Heme *x* may be the *n*-side heme described spectroscopically in *Chlorella sorokiana* (*27*, *28*) and implied by mass spectrometry (*18*). Heme *x* is covalently linked to the protein by a single thioether bond to invariant Cys^{35} in helix A of cytochrome b_6. Cys^{35} is not part of a signature sequence characteristic of c-type cytochromes, in which the heme has thioether bonds to two cysteines and an orthogonal His ligand. The Fe of heme *x* is not coordinated by protein side chains but by a small molecule assigned as water. The water is hydrogen-bonded to a propionate side chain of heme b_n, and to the backbone amide of invariant Gly^{38} in cytochrome b_6 (Fig. 3B). The sixth coordination position is unoccupied. Heme *x* is inferred to be a universal feature of the b_6f complex, because its binding site is well conserved among b_6f sequences. Invariant Tyr^{33}, Cys^{35}, Gly^{38}, Phe^{203}, and Ile^{206} of cytochrome b_6 and Phe^{40} and Ile^{44} of subunit IV contact heme *x*. Invariant Val^{26}, Pro^{27}, Pro^{28}, His^{29}, Asn^{31}, Arg^{207}, and Gln^{209} of cytochrome b_6 line the heme-binding site.

The nearly perpendicular planes of heme *x* and heme b_n are in contact through the propionate-H_2O linkage, which implies efficient electron transfer between the two hemes and an electron transfer function for heme *x* that includes heme b_n. Heme *x* occludes heme b_n from the central quinone

exchange cavity. One face of heme *x* packs against an edge of heme b_n and the A and D helices. The other face of heme *x* contacts the central cavity and helix E of subunit IV (Fig. 3B). Heme *x* is shielded from the aqueous phase by N- terminal (residues 25 to 30) and C-terminal (residues 207 to 211) segments of cytochrome b_6.

The weak fifth coordination ligand and unoccupied sixth coordination position of heme *x* are likely to give a high-spin character to ferric heme *x*. A high-spin electron paramagnetic resonance (EPR) signal in the b_6f complex has been reported (*29*). A pyridine hemochromagen difference spectrum of *M. laminosus* cytochrome b_6f revealed an extra heme whose spectrum is red-shifted relative to that of cytochrome f (*30*).

The lipid phase. Chlorophyll a and β-carotene chromophores have been found in b_6f complexes from plant, algal, and cyanobacterial sources in an approximate 1:1:1 ratio with the protein (*31–33*). The chlorophyll is bound between helices F and G of subunit IV (Figs. 2, A and C, and 3A). In the 3.0-Å electron density map, no chlorophyll Mg ligands can be identified from protein or solvent. The chlorophyll a and heme b_n planes are parallel and approximately 16 Å apart (Fig. 4, left). The 20-carbon chlorophyll phytyl tail threads through the *p*-side redox chamber into the central cavity (Figs. 2C and 3A).

A molecule of 9-*cis* β-carotene is inserted near the center of the transmembrane region between the helices of PetL and PetM, in contact with the B, E, and PetG helices (Fig. 2, B and C). It is oriented obliquely to the membrane plane and chlorophyll a. It is too far from chlorophyll a (at least 14 Å) for effective quenching of the chlorophyll excited triplet state, the presumed function of bound β-carotene (*34*). The function of the chlorophyll a is unknown, but it may fill structure gaps, similarly to bound lipids in membrane proteins (*35*).

An endogenous plastoquinone molecule is bound at the *n* side of each central cavity adjacent to heme *x*, identifying this as the Q_n site. The head group near the cavity floor is in contact with heme *x*, and the isoprenoid chain extends upward into the cavity (Figs. 2D and 3A). Two molecules of DOPC, the synthetic lipid that is essential for crystallization, are bound in each cavity (not shown) and appear to provide structural support for the cavity. One lipid is bound with its head group at the cavity roof and the aliphatic chains extending down into the complex. The head group of the second lipid is adjacent to plastoquinone at the cavity floor. Although the phosphatidylcholine head group is not found in *M. laminosus*, the added lipid does not alter

Table 1. Crystallographic data.

Data set	TDS	DBMIB	Native
X-ray source	APS SBC-19ID	SPring-8 BL44XU	SPring-8 BL44XU
Wavelength (Å)	1.0332	0.9000	0.9000
Cell constants ($P6_1$)			
a, b (Å)	157.5	156.4	156.6
c (Å)	360.4	363.3	361.8
Resolution* (Å)	3.0 (3.11–3.0)	3.4 (3.52–3.4)	3.4 (3.52–3.4)
Unique reflections (#)	100,622	65,488	67,633
Redundancy	7.0	3.1	7.8
Completeness* (%)	99.8 (100.0)	95.0 (87.7)	98.4 (96.4)
†R_{merge}*	0.068 (0.540)	0.068 (0.449)	0.089 (0.372)
$<I/\sigma_I>$*	17.9 (2.2)	13.7 (1.8)	18.0 (3.6)
‡R_{cryst}	0.259	0.326	0.256
‡R_{free}	0.346	0.361	0.336
RMSD bonds (Å)	0.011	0.015	0.013
RMSD angles (°)	1.9	1.9	1.9
Mean B values (Å²)	88	121	96

*Values in parentheses apply to the highest-resolution shell. †$R_{merge} = \Sigma_h \Sigma_i |I_i(h) - <I(h)>| / \Sigma_h \Sigma_i I_i(h)$, where I_i is the i^{th} measurement of reflection h and $<I(h)>$ is a weighted mean of all measurements of h. ‡$R = \Sigma_h |F_{obs}(h) - F_{calc}(h)| / \Sigma_h |F_{obs}(h)|$. R_{cryst} and R_{free} were calculated from the working and test reflection sets, respectively. The test set comprised 3% of the total reflections not used in refinement.

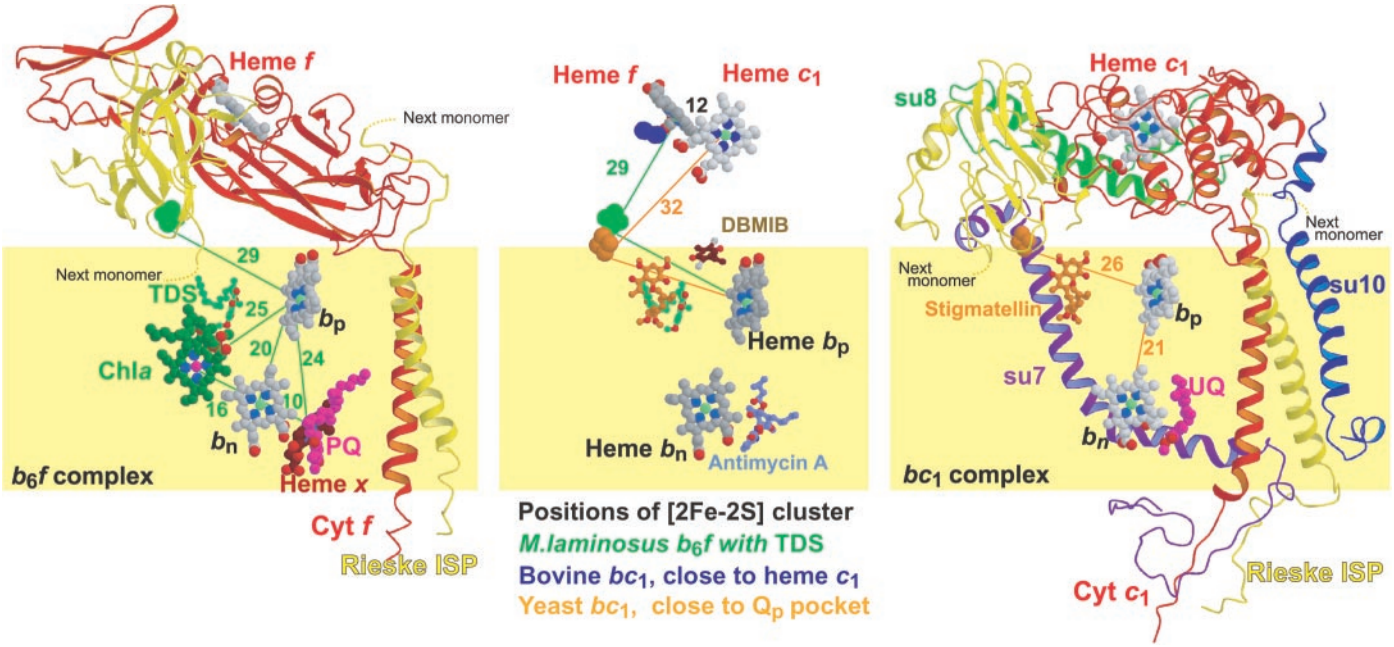

Fig. 4. Comparison of cytochrome b_6f (**left**) and yeast mitochondrial bc_1 (**right**) monomers, showing inhibitor binding sites and different positions of cytochromes f and c_1 and the [2Fe-2S] clusters. Positions of the [2Fe-2S] clusters and the c-type cytochromes of the superimposed complexes are shown in the center. *p*-side inhibitors of the b_6f complex are TDS (left, center), and DBMIB (**center**). The *p*- and *n*-side inhibitors of the bc_1 complex are stigmatellin (center, right) and antimycin A (center). The binding site of DBMIB is near Glu^{78} in the conserved ef loop of subunit IV. Color code is as in Fig. 2A.

the in vitro activity of the complex or the efficiency of quinone-analog inhibitors (*30*).

Quinone-analog binding: *p* side. Two *p*-side quinone-analog inhibitors, TDS and 2,5-dibromo-5-methyl-6-isopropyl-benzoquinone (DBMIB), were separately cocrystallized with the b_6f complex. In the 3.0 Å structure of a co-crystal with TDS, the head group of TDS binds at the roof of the central cavity on the *p* side of the complex, and its 13-carbon tail extends through a portal into the Q_p pocket (Figs. 2, B and D, and 3A). This orientation is opposite to that described for stigmatellin in the cytochrome bc_1 complex (*17*) (Fig. 4, center), where the head group directly contacts the [2Fe-2S] cluster, while its tail extends into the central cavity. In the b_6f complex, the TDS head group is 20 Å from the [2Fe-2S] cluster. TDS inhibition may be due to occlusion of the Q_p portal, a new mode of *p*-side inhibition by the quinone analogs. Restriction of the portal by the chlorophyll phytyl tail raises the problem of tight passage of plastoquinone through the portal. The binding of plastoquinone on the *n* side of the large cavity and the quinone-analogue inhibitor TDS on the *p* side (Fig. 2D) illustrates the transfer of plastoquinone between the *p* and *n* sides of different monomers.

The other inhibitor, DBMIB, binds between the E and F transmembrane helices of subunit IV in a region of the Q_p pocket that is highly conserved in b_6f and bc_1 complexes. The DBMIB binding site, identified independently in several co-crystal data sets, is also approximately 20 Å from the [2Fe-2S] cluster (Fig. 4, center). The site in the crystal structure may be a high-affinity site with little effect on the [2Fe-2S] EPR signal (*36*).

Comparison with the cytochrome bc_1 complex. The intercofactor distances (Fig. 4) and the organization of 8 of the 13 transmembrane helices (A to D in cytochrome b_6, E and F in subunit IV, ISP, and cytochrome f) are similar in the b_6f and bc_1 complexes. The RMSD for Cα atoms is 2.0 Å for helices A to F of the dimer. The G helix of subunit IV has a position intermediate to the G and H helices of cytochtrome bc_1, and helices F and G are further apart in cytochrome b_6f in order to accommodate the chlorophyll a (Figs. 2C and 3A). The four small subunits of cytochrome b_6f form a hydrophobic "picket fence" around the core subunits (Fig. 2, A and C) and occupy positions unlike any subunits of cytochrome bc_1.

Hemes b_p and b_n are oriented identically in the b_6f and bc_1 complexes (1.1 Å RMSD for the four b-heme Fe atoms of the dimer). Relative to cytochrome b in the bc_1 complex, cytochrome b_6 has an additional residue (Thr^{188}) between the two histidine ligands in the D helix (*23*). Thr^{188} is accommodated by a 25° kink in the helix, centered at Phe^{189} (Fig. 3A). Heme *x* in cytochrome b_6f is located at the same position as the *n*-side ubiquinone and antimycin A binding site in the bc_1 complex (Fig. 4, center). Thus, the two complexes have different Q_n sites. This also explains why no inhibitors of *n*-side electron transfer in the cytochrome b_6f complex have been identified that are similar to antimycin A.

Though the central cavity is a prominent feature of both the b_6f and bc_1 complexes, there are differences. Access to the Q_p and Q_n sites within the cavity is quite different in the two complexes. Because of constriction of the portal by the chlorophyll phytyl tail, the Q_p site of cytochrome b_6f is less accessible than the Q_p site of the bc_1 complex. In contrast, the Q_n site is more accessible in cytochrome b_6f, because it is not in an enclosed pocket as in cytochrome bc_1. The central cavity is more exposed to the quinone pool in the center of the membrane bilayer in the b_6f than in the bc_1 complex, where the entrance is narrowed by small subunits 10 and 11 (*15*, *37*). Instead, the F and ISP transmembrane helices define the mouth of the cavity in the b_6f complex (Fig. 2, C and D).

***p*-side extrinsic domains: cytochrome f.** The extrinsic domains of the b_6f and bc_1 complexes are strikingly different. Just as cytochromes f and c_1 are unrelated (*19*), so

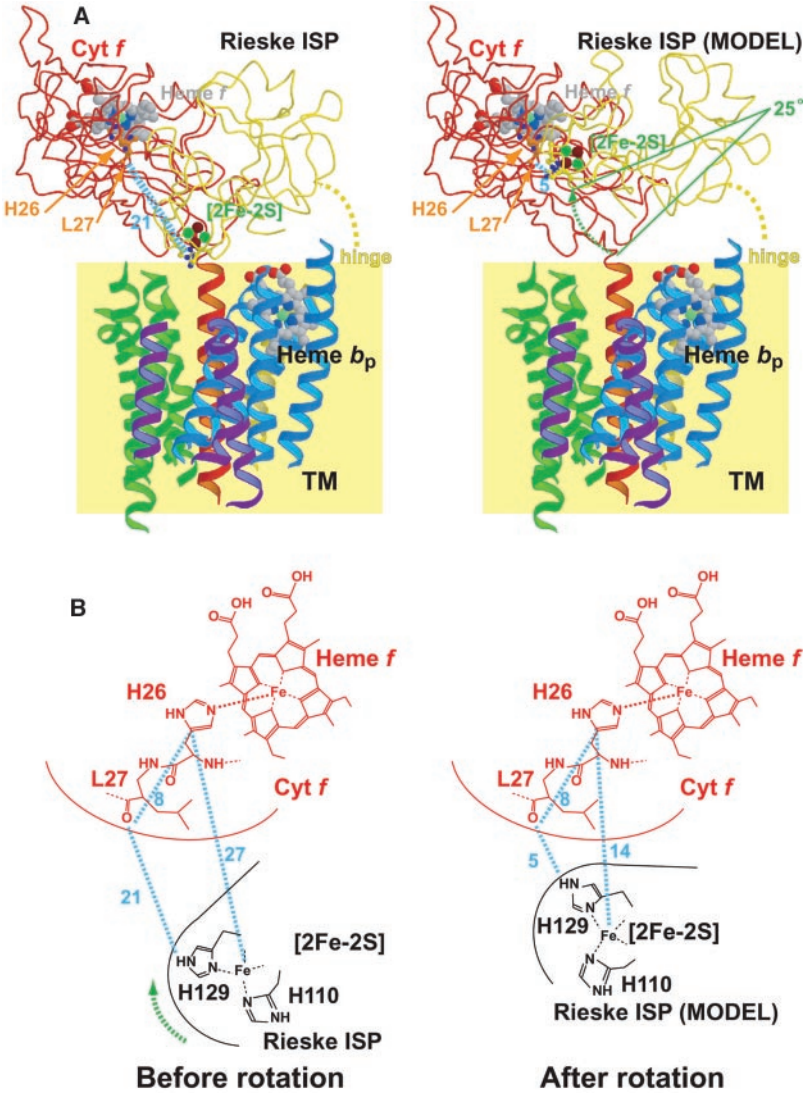

Fig. 5. Hypothesis for pathway of electron transfer between ISP and cytochrome f. (**A**) Side views showing the cytochrome f and ISP extrinsic domains in the crystal structure (left) and the model in which the soluble domain of ISP is rotated by 25° toward cytochrome f (right). His^{26} and Leu^{27} (orange) are shown in a ball-and-stick model. Distances between Leu^{27} (cytochrome f) and His^{129} (ISP) are shown as dotted lines: 21 Å in the crystal structure and 5 Å in the model after 25° rotation. The rotational trajectory of the [2Fe-2S] cluster in the proposed model is shown as a dotted arrow. Color code is as in Fig. 2A. (**B**) Schematic drawing around the [2Fe-2S] cluster and cytochrome f heme, showing the distances in the experimental and model structures.

their hemes map to positions differing by 12 Å relative to the transmembrane b hemes (Fig. 4, center). Cytochrome f consists of two extrinsic structural domains (Fig. 4, left). The larger heme-binding domain occupies a position similar to part of the cytochrome c_1 extrinsic domain. The small domain occupies a position analogous to subunit 8 in cytochrome bc_1. There is no analog in the b_6f complex for subunit 7, a pedestal for subunit 8 (Fig. 4, right). Cytochrome f also lacks intermonomer contacts, which exist in cytochrome c_1. The contrast of the 48° angle between heme and membrane planes in the present structure, in which cytochrome f is reduced, and the 30° angle when cytochrome f is oxidized (*38*), suggests the possibility of movement of the cytochrome. However, the structure has not provided evidence for such motion, as the large heme-binding domain of cytochrome f conforms to the molecular twofold symmetry of the core of the complex. The small domain exhibits a 5° difference in hinge angle between the monomers of the complex, similar to its variability in the structures of isolated cytochrome f (*19*–*21*).

***p*-side electron transfer.** Large-scale motion of the ISP extrinsic domain is essential for cytochrome bc_1 function (*14*). The ISP extrinsic domain is flexibly tethered to its transmembrane helix and, in different crystal structures, lies in extreme positions that vary between proximal to the *p*-side quinol binding niche and proximal to the heme of cytochrome c_1 (Fig. 4, center) (*14*, *15*). The extrema differ by a 60° rotation, resulting in a net displacement of the [2Fe-2S] cluster by 16 Å (*14*). Among the isomorphous crystal structures reported here, no such changes are seen for the ISP in cytochrome b_6f. Different motional trajectories may be employed in the b_6f and bc_1 complexes, because the extrinsic domains of cytochrome f and c_1 dictate different interactions of the [2Fe-2S] cluster. In the present structure, the [2Fe-2S] cluster and cytochrome f heme Fe atoms are separated by 29 Å (Fig. 4), which is too long for electron transfer to occur at a competent rate. Therefore, the extrinsic domain of the ISP and/or cytochrome f must move.

In the crystal structure, the [2Fe-2S] cluster points away from cytochrome f, into the Q_p site (Fig. 5A). Therefore, motion of at least the ISP is necessitated by the inaccessibility of the [2Fe-2S] cluster and its distance from the cytochrome f heme. Motion is consistent with the different ISP orientations in the two monomers. When transformed by the molecular twofold symmetry, the superimposed ISP extrinsic domains differ by a 12° rotation and approximately 2 Å translation parallel to the membrane plane. Motion is also consistent with the flexibility in the multiglycine hinge region of the ISP in cytochrome b_6f. Mutagenesis of the hinge region implied that less movement of ISP is required in cytochrome b_6f than in the bc_1 complex (*39*). A 14 Å displacement of the [2Fe-2S] cluster can be achieved by rotation of the ISP by 25° toward cytochrome f, which shortens the distance between the [2Fe-2S] cluster and the His^{26} heme ligand to 14 Å. This would bring the [2Fe-2S] cluster into apposition with the backbone carbonyl of Leu^{27} of cytochrome f (Fig. 5, A and B). Electron transfer from this position to the imidazole of the His^{26} heme Fe ligand would be very efficient, because it would involve transfer through a pathway of eight covalent bonds (Fig. 5B) (*40*) and a distance of less than 8 Å between the carbonyl of Leu^{27} and the His^{26} imidazole ring (*41*).

Heme *x* and cyclic electron transfer. Heme *x* does not appear to be required for Q-cycle function (Fig. 2A), because the other elements of the Q cycle (hemes b_p and b_n) are identically oriented in the b_6f and bc_1 complexes, have identical interheme distances, and have similar hydrophobic environments between hemes. However, the oxygenic photosynthetic electron transport chain also carries out ferredoxin-dependent cyclic electron transport, whose purpose is to support levels of adenosine triphosphate relative to NADPH needed for carbon fixation (Fig. 1). In cyanobacteria, the cyclic pathway is dominant at physiological CO_2 concentrations (0.03%) or low illumination levels (*42*). Heme *x*, which can readily contact plastoquinone in the central cavity (Fig. 3A), may be the hitherto elusive ferredoxin-plastoquinone reductase inferred to be essential for this activity. The positive stromal-side surface potential of cytochrome b_6f would facilitate docking of anionic ferredoxin to the stromal (*n*) side of the complex near heme *x*.

Determination of the 3.0 Å structure of the cytochrome b_6f complex completes the structural description of the photosynthetic electron transport chain, extends the high-resolution structural description of the family of cytochrome bc complexes, identifies a new heme cofactor, and describes the structural changes that have occurred in and around the central quinone exhange cavity in response to the demands of photosynthesis.

References and Notes

1. W. A. Cramer, D. B. Knaff, in *Energy Transduction in Biological Membranes* (Springer-Verlag, New York, 1991), chap. 6.
2. T. Kallas, in *The Molecular Biology of Cyanobacteria*, D. A. Bryant, Ed. (Kluwer Academic, Dordrecht, Netherlands, 1994), pp. 259–317.
3. W. A. Cramer *et al.*, *Annu. Rev. Plant Physiol. Plant Mol. Biol.* **47**, 477 (1996).
4. G. Hauska, M. Schütz, M. Büttner, in *Oxygenic Photosynthesis: The Light Reactions*, D. R. Ort, C. F. Yocum, Eds. (Kluwer Academic, Amsterdam, 1996).
5. P. Jordan *et al.*, *Nature* **411**, 909 (2001).
6. A. Zouni *et al.*, *Nature* **409**, 739 (2001).
7. N. Kamiya, J.-R. Shen, *Proc. Natl. Acad. Sci. U.S.A.* **100**, 98 (2003).
8. P. Rich, *Biochim. Biophys. Acta* **768**, 53 (1984).
9. B. L. Trumpower, *J. Biol. Chem.* **265**, 11409 (1990).
10. D. Kramer, A. R. Crofts, *Biochim. Biophys. Acta* **1183**, 72 (1993).
11. E. A. Berry, M. Guergova-Kuras, L.-S. Huang, A. R. Crofts, *Annu. Rev. Biochem.* **69**, 1005 (2000).
12. P. Joliot, A. Joliot, *Proc. Natl. Acad. Sci. U.S.A.* **91**, 1034 (1994).
13. D. Xia *et al.*, *Science* **277**, 60 (1997).
14. Z. Zhang *et al.*, *Nature* **392**, 677 (1998).
15. S. Iwata *et al.*, *Science* **281**, 64 (1998).
16. H. Kim *et al.*, *Proc. Natl. Acad. Sci. U.S.A.* **95**, 8026 (1998).
17. C. Hunte, J. Koepke, C. Lange, T. Roβmanith, H. Michel, *Structure* **8**, 669 (2000).
18. J. P. Whitelegge, H. Zhang, R. Taylor, W. A. Cramer, *Mol. Cell. Proteomics* **1**, 816 (2002).
19. S. E. Martinez, D. Huang, A. Szczepaniak, W. A. Cramer, J. L. Smith, *Structure* **2**, 95 (1994).
20. C. J. Carrell *et al.*, *Biochemistry* **38**, 9590 (1999).
21. G. Sainz *et al.*, *Biochemistry* **39**, 9164 (2000).
22. C. J. Carrell, H. Zhang, W. A. Cramer, J. L. Smith, *Structure* **5**, 1613 (1997).
23. W. R. Widger, W. A. Cramer, R. G. Herrmann, A. Trebst, *Proc. Natl. Acad. Sci. U.S.A.* **81**, 674 (1984).
24. H. Zhang, G. Kurisu, J. L. Smith, W. A. Cramer, *Proc. Natl. Acad. Sci. U.S.A.* **100**, 5160 (2003).
25. G. von Heijne, *Annu. Rev. Biophys. Biomol. Struct.* **23**, 167 (1994).
26. D. Stroebel *et al.*, personal communication.
27. J. Lavergne, *Biochim. Biophys. Acta* **725**, 25 (1983).
28. P. Joliot, A. Joliot, *Biochim. Biophys. Acta* **933**, 319 (1988).
29. V. Schünemann, A. X. Trautwein, J. Illerhaus, W. Haehnel, *Biochemistry* **38**, 8981 (1999).
30. H. Zhang, unpublished data.
31. D. Huang *et al.*, *Biochemistry* **33**, 4401 (1994).
32. Y. Pierre *et al.*, *J. Biol. Chem.* **272**, 21901 (1997).
33. H. Zhang, D. Huang, W. A. Cramer, *J. Biol. Chem.* **274**, 1581 (1999).
34. N. J. Turro, in *Molecular Photochemistry* (Benjamin, Reading, MA, 1965), pp. 92–134.
35. R. M. Garavito, S. Ferguson-Miller, *J. Biol. Chem.* **276**, 32403 (2001).
36. A. G. Roberts, D. M. Kramer, *Biochemistry* **40**, 13407 (2001).
37. X. Gao *et al.*, *Biochemistry* **41**, 11692 (2002).
38. A. Riedel, W. Rutherford, G. Hauska, A. Muller, W. Nitschke, *J. Biol. Chem.* **266**, 17838 (1991).
39. J. Yan, W. A. Cramer, *J. Biol. Chem.* **278**, 20925 (2003).
40. H. B. Gray, J. R. Winkler, *Annu. Rev. Biochem.* **65**, 537 (1996).
41. C. C. Moser *et al.*, *Nature* **355**, 796 (1992).
42. J. Zhao *et al.*, *Mol. Microbiol.* **9**, 183 (1993).

43. We thank J. Yan for sequences of *M. laminosus petC* and *petD*; J. Bolin, A. Friedman, D. Krogmann, and L. Sherman for helpful discussions; P. Rich for a gift of TDS; the staff of beamlines BioCARS 14BM-C and SBC 19ID at the Advanced Photon Source for assistance; and the staff at SPring-8 BL44XU for beam time. Studies were supported by NIH grant GM-38323 (W.A.C.), a Japanese Ministry of Education Fellowship (G.K.), the U.S. Department of Energy (APS-SBC), and the NIH (APS BioCARS). Coordinates are available from the Protein Data Bank with accession code 1UM3.

Supporting Online Material

www.sciencemag.org/cgi/content/full/1090165/DC1
SOM Text
Figs. S1 and S2
Table S1
References and Notes

6 August 2003; accepted 24 September 2003
Published online 2 October 2003;
10.1126/science.1090165
Include this information when citing this paper.